

A probabilistic approach for the classification of earthquakes as ‘triggered’ or ‘not triggered’

Application to the 13th Jan 1976 Kópasker Earthquake on the Tjörnes Fracture Zone, Iceland

Luigi Passarelli · Francesco Maccaferri ·
Eleonora Rivalta · Torsten Dahm ·
Elias Abebe Boku

Received: 30 June 2011 / Accepted: 23 February 2012
© Springer Science+Business Media B.V. 2012

Abstract The occurrence time of earthquakes can be anticipated or delayed by external phenomena that induce strain energy changes on the faults. ‘Anticipated’ earthquakes are generally called ‘triggered’; however, it can be controversial to label a specific earthquake as such, mostly because of the stochastic nature of earthquake occurrence and of the large uncertainties usually associated to stress modelling. Here we introduce a combined statistical and physical approach to quantify the probability that a given earthquake was triggered by a given stress-inducing phenomenon. As an example, we consider an earthquake that was likely triggered by a natural event: the $M = 6.2$ 13 Jan 1976 Kópasker earthquake on the Grímsey lineament (Tjörnes Fracture Zone, Iceland), which occurred about 3 weeks after a large dike injection in the nearby Krafla fissure swarm. By using Coulomb stress calculations and the rate-and-state earthquake nucleation theory, we calculate the likelihood of the earthquake in a scenario that contains only the tectonic background and excludes the dike and in a scenario that includes the dike but excludes the background. Applying

the Bayes’ theorem, we obtain that the probability that the earthquake was indeed triggered by the dike, rather than purely due to the accumulation of tectonic strain, is about 60 to 90 %. This methodology allows us to assign quantitative probabilities to different scenarios and can help in classifying earthquakes as triggered or not triggered by natural or human-induced changes of stress in the crust.

Keywords Triggered and induced seismicity · Bayesian statistics · Dike-induced stress changes · Rifting · Tjörnes fracture zone

1 Introduction

The north volcanic zone of Iceland and the Kolbeinsey ridge, two consecutive active Mid-Atlantic ridge segments, are connected by the Tjörnes Fracture Zone (TFZ; see Fig. 1). The TFZ is a 120-km-long and 80-km-wide WNW trending en-echelon transform fault zone composed of three main sub-parallel lineaments: the Grímsey lineament (GL) to the north, the Husavík Flatey fault (HFF) to the centre and the Dalvík lineament (DL) to the south (Rögnvaldsson et al. 1998; Stefansson et al. 2008). In the area of the TFZ, the plate spreading rate is about 2 cm/year in the N112°E direction, subdivided into 66 %

L. Passarelli (✉) · F. Maccaferri · E. Rivalta ·
T. Dahm · E. Abebe Boku
Institute of Geophysics, University of Hamburg,
Bundesstr. 55, 20146 Hamburg, Germany
e-mail: luigi.passarelli@zmaw.de

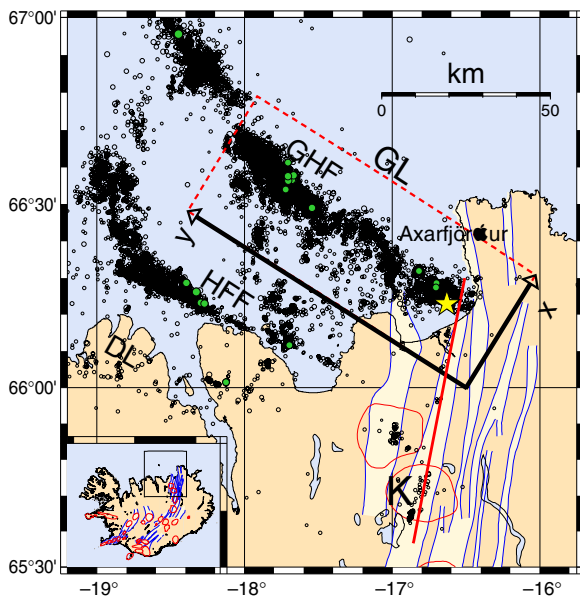


Fig. 1 Map of the epicentres of $M > 1.5$ earthquakes from Jan 1995 to Jan 2010 in the Tjörnes Fracture Zone, Iceland (see inset in the bottom left for location). $M > 4$ earthquakes are plotted as green dots. The location of the 13 Jan 1976 earthquake is indicated with a yellow star. The area of the Grímsey lineament (GL) is outlined by a rectangle, on which all calculations are carried out. Other seismic areas include the Husavík Flatey fault (HFF) and the Dalvík lineament (DL). Fissure swarms, Krafla central volcano (K) and other volcanic centres are also indicated by thin blue and red lines, respectively. The thick red solid line indicates the extent of the fissures induced by the 1975–1984 rifting event at Krafla. GHF is the Grímsey hydrothermal field

on the GL and 34 % on the HFF (Geirsson et al. 2006; Metzger et al. 2011). The TFZ is very seismically active, with the seismicity being generally diffused rather than focussed on specific fault planes. Microseismicity on the GL and some other areas of the TFZ is associated primarily to intrusive magmatic or hydrothermal activity (Riedel et al. 2005; Hensch et al. 2008; Stefansson et al. 2008); large events, with magnitude, M up to 7, also occur but are rare (Rögnvaldsson et al. 1998). Microearthquakes on TFZ, located by the Icelandic Seismic Lowland network (SIL) since 1994, tend to cluster on NS trending left-lateral fault planes (Rögnvaldsson et al. 1998). Stefansson et al. (2008) used the pattern of microearthquake activity and other evidence to re-view fault planes for large historical earthquakes

and infer the role of fluids and pore pressure on the seismic activity and tectonics in the area. Notable seismic events in the last 150 years include a major earthquake sequence on the HFF in 1872, with two $M = 6.3$ events, a $M = 7.0$ earthquake (Halldórson 2005) on the GL (1910), a $M = 6.3$ event on the DL (1934) and a $M = 6.2$ strike-slip earthquake on 13 Jan 1976 on the eastern end of GL, which is the focus of the present study (Rögnvaldsson et al. 1998).

This earthquake followed a diking event, which started a few weeks earlier on 20 Dec 1975 and marked the beginning of the 1975–1984 rifting event at Krafla volcano. The dikes, fed by a magma chamber at 3 km depth below the central volcano, propagated to the north and to the south along a ~ 80 -km-long fissure swarm, ranging from south of lake Mývatn to the north coast of Axarfjörður and terminating into a junction with the GL. Krafla caldera is located ~ 60 km south of the northern end of the rift zone (see Fig. 1). The seismicity induced by the intrusions suggests a propagation velocity of 1 to 2 m/s from the reservoir (Einarsson and Brandsdóttir 1980); the hypocentres reached ~ 10 km focal depth. The previous rifting episode at Krafla had occurred in the southern part of the rift in 1725 to 1729 (Björnsson 1985) and probably did not open into the GL junction. Before 1725, the last large rifting episode had occurred around year 900, this time probably opening into the GL (Stefansson et al. 2008).

Dike injections induce a stress change in the surrounding rocks, which is particularly large in the proximity of the dike tips and in a dog-bone pattern around the dike (Hill 1977). Such injections are sometimes responsible for massive induced and triggered seismicity (Toda et al. 2002). The Dec 1975 diking event is one of the largest in the last 40 years and caused a large rift extension of up to 3 m over a rift zone several tens of kilometres long; not surprisingly, the Kópasker earthquake is generally held as ‘triggered’ by it (Buck et al. 2006).

The last decade has seen a lot of progress in understanding static stress transfer, a process through which large earthquakes may trigger other large earthquakes nearby (Harris 1998;

Stein 1999; King and Cocco 2000). Some studies look into the interaction between doublets of large events; others investigate into sequences of earthquakes in large fault zones or into mainshock/aftershock sequences, while others (Jacques et al. 1996; Cayol et al. 2000; Hill et al. 2002; Toda et al. 2002; Feuillet et al. 2006) examine qualitatively the patterns of seismicity associated with dike injections or volcanic activity in general. A small but growing number of quantitative studies (Lengliné et al. 2008; Dieterich et al. 2000; Segall et al. 2006) do compare seismic rates following a stress-inducing event with rates calculated through earthquake nucleation models, such as the rate-and-state formulation (Dieterich 1994), but generally causal relationships between events are still simply based on qualitative comparisons of maps of changes in the Coulomb failure function (ΔCFF) with the locations of the earthquakes under consideration. However, the parameters involved in the calculation of stress and seismic rate changes are numerous and affected by significant uncertainties; small variations in the model parameters or different choices in the stress modelling may cause significant changes in the Coulomb stress (including changes from positive to negative or vice versa) in large areas. Also, earthquake processes and nucleation models have a strong stochastic component. It is therefore impossible to ascertain with 100 % confidence whether an earthquake was triggered or not by a given event; this assessment should be rather carried out probabilistically.

Here we present an approach developed to assess the probability that an earthquake following a stress-inducing event was triggered by it and describe it step by step as we apply it to the Dec 1975–Jan 1976 diking/earthquake sequence in the Krafla fissure swarm and TFZ. The approach involves comparing the probabilities of two mutually exclusive hypotheses:

- Tectonic scenario (T)—the earthquake originated only from the tectonic load of the region (not triggered)
- Dike scenario (D)—the earthquake occurred only as a consequence of the dike stress perturbation (triggered)

Those probabilities are obtained by applying Bayes' theorem to the likelihood of the earthquake in the two scenarios, calculated as follows: (1) We use dislocation theory to calculate the Coulomb stress induced by the dike, (2) we employ the rate and state model to calculate the correspondent changes in seismicity rate, (3) we calculate the spatial probability density that an earthquake of that magnitude occurs on that day in the area and (4) we combine the information on the location (epicentre and uncertainty) with this probability into the likelihood of the earthquake.

After discussing and quantifying the possible sources of error, we indicate how our model can be used to assess the probability that earthquakes of a given magnitude range in a given time interval and area were triggered by specific natural phenomena or human activities (e.g. mining, extraction of oil or gas, injection of fluids).

2 Bayesian assessment of triggering probability

We define an earthquake as 'not triggered' when its occurrence is a consequence of the regional tectonic load alone; we define it as 'triggered' when its occurrence is anticipated to the observed onset time by external factors, in this specific analysis the dike-induced stress change. In general, a third case is possible: The earthquake would have never occurred without the dike, and the energy released by the earthquake was provided entirely by the dike. Such an earthquake may be called 'induced'. As our target earthquake was large and occurred on a major fault system, we consider this option very unlikely with respect to a triggered scenario, and we neglect it, but in general, it is a possibility that can be considered with the present approach.

Our aim is to evaluate the posterior probability of each hypothesis, in turn the tectonic scenario T and the dike scenario D , given (conditional to) the earthquake occurrence E , that is, $p(D | E)$ and $p(T | E)$. At this purpose, we apply Bayes' theorem to combine the probability of occurrence (likelihood) of the earthquake for each scenario ($p(E | D)$ and $p(E | T)$), which we estimate from

a physical and statistical modeling of the seismicity with an assigned ‘a priori’ probability $p(D)$ and $p(T)$ for each scenario. For the Dike scenario:

$$p(D | E) = \frac{p(D)p(E | D)}{p(D)p(E | D) + p(T)p(E | T)} \quad (1)$$

and for the complementary Tectonic scenario:

$$\begin{aligned} p(T | E) &= 1 - p(D | E) \\ &= \frac{p(T)p(E | T)}{p(D)p(E | D) + p(T)p(E | T)} \quad (2) \end{aligned}$$

The most likely scenario is the one with the highest value of posterior probability. For example, the inequality $p(D | E) > p(T | E)$ translates into the inequality $p(D)p(E | D) > p(T)p(E | T)$. If we find the inequality to hold, the Dike scenario has higher probability than the Tectonic scenario, and we shall conclude that the event was triggered with probability $p(D | E)$. See Cesca et al. (2011) for an application of the proposed scheme to a different classification problem.

The probabilities from Eqs. 1 and 2 will be time dependent in general, even if time is not explicitly indicated in the formulation. For example, the probability of triggering, $p(D | E)$, is expected to approach zero for times much larger than the time of dike intrusion, when the dike-induced stresses will have already been released. The time evolution of the triggering probability will be modulated by the particular time-dependent seismicity modelling used, as discussed later in the paper.

We postpone to Section 3 through Section 5 a description of how we calculate the probabilities $p(E | D)$ and $p(E | T)$. First, we discuss the a priori probability for each scenario.

The a priori probability indicates the probability of each scenario relying solely on information detached from the data one uses to calculate the likelihood. Ideally, a reasonable prior probability could be assigned as the relative frequency of large earthquakes triggered by dikes out of all the earthquakes in the same magnitude range occurring in the same area. An analogue calculation was carried out by Parsons (2002), who compiled a catalogue of positive or negative shear stress changes on the fault area sites of large earthquakes ($M > 7$) due to other earthquakes in the same catalogue. He estimated that triggered

earthquakes, defined there as earthquakes occurring on fault planes affected by a shear stress increase induced by other earthquakes, are at least 8 % in his catalogue. Unfortunately, there is a lack of similar information on earthquakes triggered by dikes (which mainly induce changes in compression rather than in shear stress) or for our target area. If available, the relative frequency of dike-induced seismicity, observed just before the target earthquake (this can be obtained by removing the tectonic background, r , from the observed seismicity rate, R , and then dividing by R for normalisation), could be used as an estimate of the a priori probability of triggering, if of course the same data were not employed already to constrain the physical and statistical modelling for the calculation of $P(E | D)$: The same data should not be used twice, to estimate the prior and to fit the seismicity model. For the Kópasker earthquake, we lack robust sources of a priori information and prefer to use a so-called non-informative a priori probability for each scenario. In probabilistic term, the maximum a priori ignorance (non-informative priors in Bayesian Statistics) can be expressed assigning $p(D) = p(T) = 0.5$, meaning that each scenario is equally likely to happen a priori; this crude estimate will improve when, as typical in Bayesian studies where posteriors from earlier studies are used as informative priors, we gather more information on $p(D)$ and $p(T)$.

The purpose of the next sections is to calculate the probabilities $p(E | D)$ and $p(E | T)$. The first step is to estimate the impact of the dike-induced stress field on the seismicity.

3 Stress modelling

3.1 Geophysical constraints

We model the stress field induced by the 20 Dec 1975 dike intrusion using dislocation theory. The dike is modelled as a boundary element crack in an infinite elastic medium, in plain strain approximation (the dislocations have infinite extension along the vertical coordinate, z). We employ these approximations, rather than a full 3D model, because of the large uncertainties in the vertical

extension of the dike and in the depths of the dike top and earthquake hypocentre.

Hainzl et al. (2010) estimated the failure of accounting for the distributed slip on fault planes as one of the major sources of error for earthquake-induced models that use the Coulomb failure function because slip heterogeneity may significantly change the stress pattern. For a magma intrusion, the analogy of a non-uniform slip distribution is a non-uniform opening of the dike walls. Therefore, we use geodetic observations and physical considerations in order to constrain distributed opening on the dike and reduce the error in our ΔCFF model. We set as boundary condition the overpressure, ΔP , along the coordinate s of the dike strike:

$$\Delta P(s) = P_{\text{mag}} - P_{\text{lit}}(s) + \sigma_n, \tag{3}$$

where P_{mag} is the magma pressure (constant along dike strike for a static dike), $P_{\text{lit}}(s)$ is the lithostatic pressure (varying with s owing to topography) and σ_n is the normal component of the tectonic stress acting on the dike, positive for extension (see Table 1 for the numerical values assumed in the calculation). P_{mag} and $P_{\text{lit}}(s)$ can be chosen according to different approaches or assumptions. By carrying out calculations for four different models, we obtain an estimate of the sensitivity of the final result to the specific stress model chosen (see Section. 6 for a discussion of this and other sources of error).

Constraint on the magmatic pressure P_{mag}

A1. Following Buck et al. (2006), the overpressure at the norther tip of the dike s_t can be constrained to match the minimum driving pressure for propagation (ΔP_{min}):

$$\Delta P(s_t) = \Delta P_{\text{min}} \tag{4}$$

Table 1 Parameters employed for the dike modeling

Rock parameter	Value	Unit	Magma parameter	Value	Unit
ρ_r	3,000	kg/m ³	ρ_m	3,000	kg/m ³
μ	30	GPa	K	10	GPa
ΔP_{min}	5	MPa	A	0.11	km ²
σ_n	10	MPa	d	1	km

We assume a Poisson ratio $\nu = 0.25$ for rocks

A2. Alternatively, P_{mag} could be constrained by fixing the cross section of the dike according to published geodetic measurements for the cross-sectional area change A in the rift zone after the diking event (Tryggvason 1984). Considering the magma as a compressible fluid, we have:

$$P_{\text{mag}} = -K \frac{A - A_0}{A_0} \tag{5}$$

where A is the dike cross section at depth d that we assume equal to the measured area change in the rift zone. $A_0 > A$ represents the reference volume of the intrusion per unit height at the reference pressure set equal to zero, when the magma has bulk modulus K (Dahm 2000; Maccaferri et al. 2010).

Constraint on the lithostatic pressure $P_{\text{lit}}(s)$

B1. The lithostatic pressure depends on the topographic profile of the Krafla rift zone over the dike strike (see Fig. 2). A simple way to calculate it is:

$$P_{\text{lit}}(s) = \rho_r g (h(s) + d) \tag{6}$$

where ρ_r is the rock density, g is the acceleration due to gravity, $h(s)$ is the topography elevation above the see level and d is the depth of the dike below see level. This results in an average gradient along s of 0.2 MPa/km.

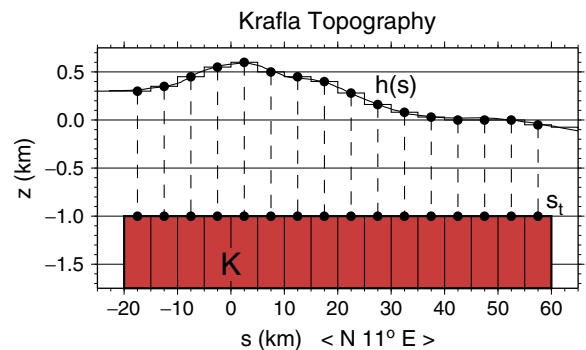


Fig. 2 Topography profile along the strike s of the propagating dike plane. The symbol K in $s = 0$ indicates the location of the Krafla caldera

B2. A second option is to calculate $P_{lit}(s)$ more precisely as the load exerted by the topography on the dike plane (again in plane strain approximation) using the analytical formulas in (Dahm 2000, “Appendix”):

$$P_{lit}(s) = \sigma_n^{tp}(s, d) + \rho_r g d \tag{7}$$

where $\sigma_n^{tp}(s, d)$ is the normal component of the stress tensor induced by the topographic load in a point s of the dike strike at depth d . The resulting average overpressure gradient along s is approximately 0.14 MPa/km.

We combine these options into four different overpressure profiles. The corresponding dike opening distributions are shown in Fig. 3. Model $M1$ is obtained by combining Eqs. 3, 4 and 6 (assumptions A1 and B1). For model $M2$, we combine Eqs. 3, 4 and 7 (assumptions A1 and B2). Model $M3$ is obtained combining Eqs. 3, 5 and 6 (A2 and B1), and model $M4$ results from Eqs. 3, 5 and 7 (A2 and B2). Note that although configurations $M3$ and $M4$ do not include a threshold pressure for fracturing the host rock, for these cases the resulting overpressure at the propagating tip of the dike is very similar to the assumed overpressures for models $M1$ and $M2$: $\Delta P(s_t) = 6.0$ MPa for case $M3$ and $\Delta P(s_t) = 4.8$ MPa for case $M4$.

These four different models give similar results both for the total cross sectional area dislocated by the dike and for the dike opening, in particular near the location of the earthquake epicentre (see Fig. 3). The tip curvature influences most the stress change close to the earthquake epicentre; the extreme scenarios producing the smallest and

largest stress change are represented by models $M1$ and $M3$, respectively.

3.2 Coulomb stress maps

In Fig. 4 (a1, b1 and a2, b2), we plot the normal and shear components of the stress induced by the dike (model $M4$) on the planes indicated by the dashed lines, oriented as the two strike directions proposed for the 13 Jan 1976 event. The two fault plane solutions have strike N32°E and N122°E (Einarsson 1987). The first fault plane solution is perpendicular to the GL, and the second is parallel to it; we will label them as \perp GL and \parallel GL, respectively. The corresponding Coulomb stress change (Fig. 4, a3 and b3) is given by:

$$\Delta CFF_1 = \sigma_s + \mu \sigma_n \tag{8}$$

where the shear stress component σ_s is positive if concordant with the slip of the relative mechanism and the normal stress σ_n is positive when tensile. Here we show the ΔCFF maps obtained by setting the friction coefficient to $\mu = 0.8$ (dry medium). We discuss the errors on the ΔCFF arising from neglecting the influence of fluids in the Section 6. As shown in Fig. 4, the earthquake hypocentre is located, within uncertainties, in the same region as the dike tip; therefore, it is important to estimate the Coulomb stress change in close proximity to the tip. The stress field due to an elementary dislocation is affected by a non-realistic singularity scaling with the inverse of the distance from the dislocation tips. We assume an upper limit to the stress that can be sustained by rocks before fault-

Fig. 3 Opening of the dike for four different boundary conditions. The vertical dashed line and the yellow region indicate the projection of the earthquake epicentre on the dike strike s and the associated Gaussian error

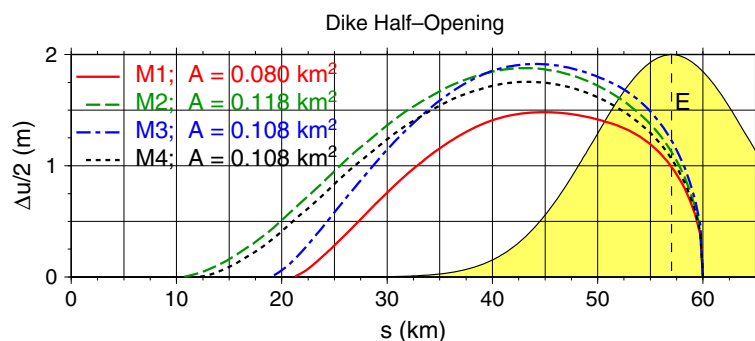
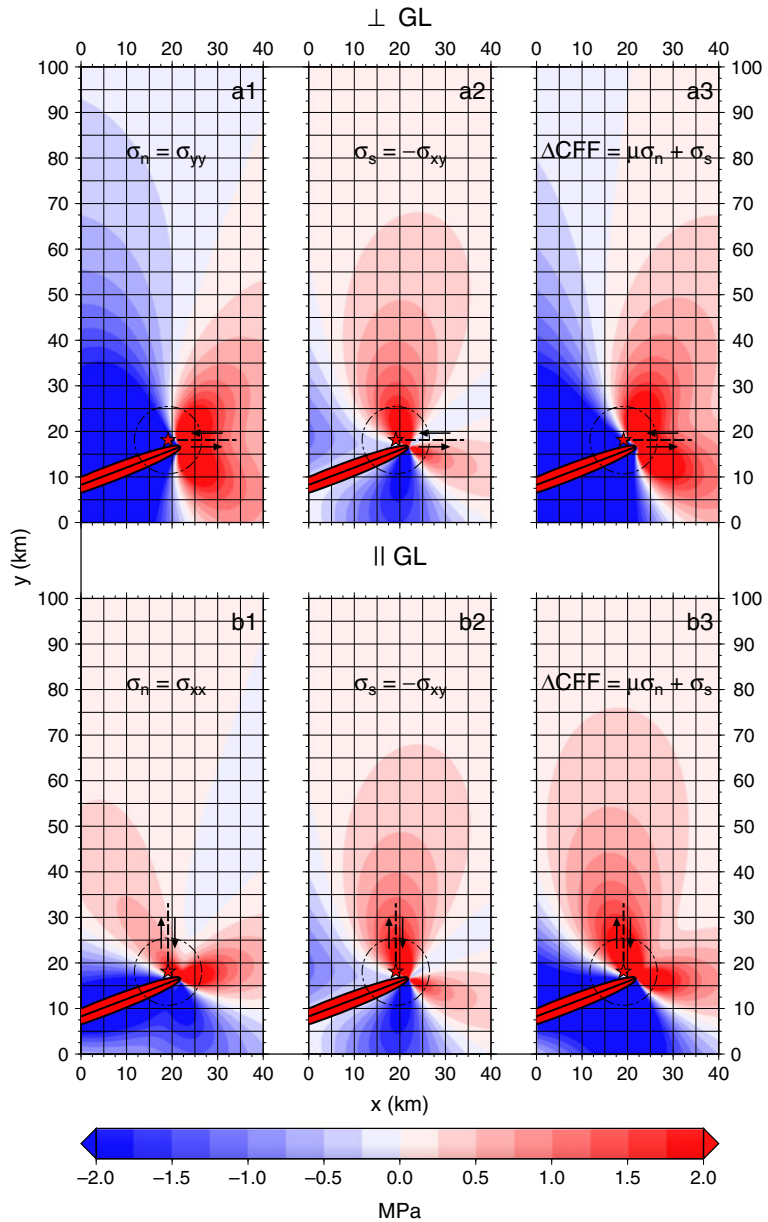


Fig. 4 *a1, a2* and *b1, b2* Normal and shear stress components on the \perp GL and \parallel GL fault plane for model M4. The Δ CFF is plotted in *a3* and *b3*. The *red stars* indicate the earthquake epicentre; the *dashed circle* represents the location error (7.5 km radius, corresponding to 1σ of the bivariate gaussian error distribution). The *horizontal* (\perp GL) and *vertical* (\parallel GL) *dashed lines* (15 km length) represent the two possible strikes of the *vertically dipping* rupture plane. The *arrows* indicate the rupture mechanism



ing, which we set equal to the minimum overpressure, ΔP_{min} , needed by the dike to propagate.

We find a positive Coulomb stress change on the fault for both different orientations of the rupture (see Fig. 4, a3 and b3). Interestingly, however, for the \perp GL orientation, it is the normal stress component that contributes most to the Δ CFF (see Fig. 4a1), implying that for a large magnitude earthquake to occur, the shear stress to be released by the rupture must have been almost

completely pre-loaded on the fault. In contrast for the \parallel GL orientation, the major contribution to the Δ CFF comes from the shear stress directly loaded on the fault by the dike (see Fig. 4b2).

4 Observed and modeled seismicity

The probability of occurrence of earthquakes can be estimated through a statistical analysis of the

earthquake catalogues. Unfortunately, the seismic catalogue for the time frame of the Krafla rifting episode is not available to us. Therefore, we can only base our statistics on the activity from 1 Jan 1995 to 31 Jan 2011 recorded by the SIL network (Icelandic Meteorological Office, <http://hraun.vedur.is/>), on the assumption that the seismicity before the rifting episode can be represented by the seismic activity that occurred from 10 years after the last dike intrusion at Krafla. The assumption introduces an approximation that we deem acceptable on account of the following considerations:

- In 1995, the stresses induced on the GL by the intruded dikes are already released (we verify this quantitatively in Section 4.3).
- No additional volcanic events occurred in the Krafla fissure swarm after the 1975–1984 rifting episode.
- No additional large earthquake occurred in the region from 1976 to present.

In other words, we assume that the seismicity recorded since 1995 on the GL can be mostly ascribed to the tectonic forces and represents the state of stress before the rifting episode. Consequently, we consider that the average seismicity rate and the parameters for the Gutenberg–Richter law estimated from the SIL catalogue are valid for the pre-rifting time period. In the following, we first present the seismic catalogue and its main features and then estimate the seismicity rate changes induced in the region by the Δ CFF by using the rate-and-state earthquake nucleation model (Dieterich 1994; Toda and Stein 2003; Cocco et al. 2010).

4.1 Statistical analysis of the seismic catalogue

For our analysis, we select all events with depth 0 to 15 km across the GL, as delineated by the rectangular area in Fig. 1. The total number of selected events is 25,464, with minimum and maximum recorded magnitude equal to -0.16 and 4.56 , respectively. The error on the magnitude is not given in the catalogue, while errors on the hypocentre locations are in the range 2–10 km

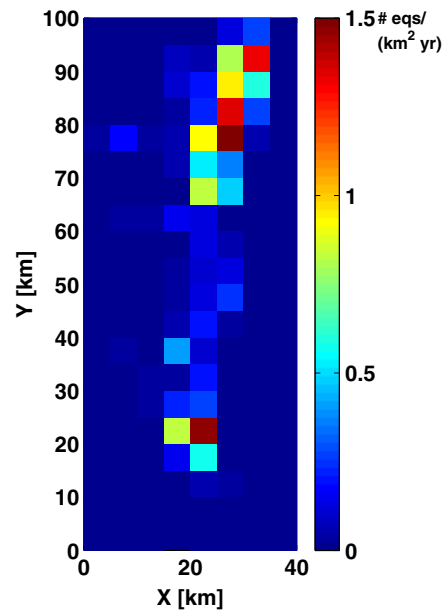


Fig. 5 Observed seismicity rate on the GL calculated over square patches of 5 km side. The most active regions are the southeastern part and the northern part of the GL, correspondent to Axarfjörður and the GHF, respectively, see Fig. 1

(Rögnvaldsson et al. 1998). The catalogue contains several earthquake swarms, which are likely related to fluid migration due to volcanic and hydrothermal activity in the region (Riedel et al. 2003, and references therein). The two most seismically active areas in the GL are the Axarfjörður area in the southeast and the Grímsey hydrothermal field (GHF), northwest of the lineament (see Figs. 1 and 5).

We find a magnitude of completeness $M_c = 1.5$ at the 95 % confidence level according to the goodness-of-fit test proposed by Wiemer and Wyss (2000) (Fig. 6). The inference on the parameters b and a of the frequency–magnitude distribution is based on the maximum likelihood estimation for grouped data proposed by Bender (1983). The data are grouped in magnitude bins of 0.1 in the range $[M_c; M_{\max}]$; we obtain $b = 1.09 \pm 0.01$, which is compatible with the spatial distribution of b values inferred by Riedel et al. (2003) for the Grímsey lineament. The error associated to the b value estimation was calculated using the Shi and Bolt (1982) relation.

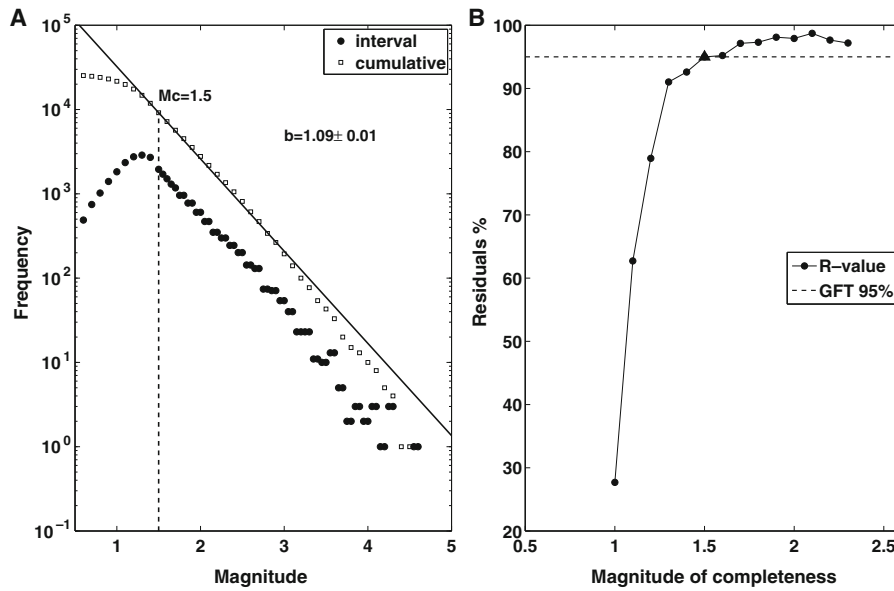


Fig. 6 Estimated Gutenberg–Richter law and magnitude of completeness, M_c , for the SIL seismic catalogue from 1 Jan 1995 to 31 Jan 2011. **a** Gutenberg–Richter estimation for magnitude grouped data (Bender 1983); the estimated a value is 4.91; *black dots* are frequency of events for grouped data with magnitude bin equal to 0.1, and *empty squares* are

the cumulative frequency. **b** Estimation of the magnitude of completeness using the goodness-of-fit test (Wiemer and Wyss 2000); the *dashed line* is the 95 % confidence level for the test, and the *black triangle* indicates the inferred magnitude of completeness M_c

4.2 Changes in seismicity rate induced by the dike intrusion

The statistics of earthquake production resulting from stress changes can be modelled using the rate and state theory (Dieterich 1994). Although it is possible to calculate the effects on the seismicity rate of an arbitrary stress history, since we are lacking details on the time-dependent dike-induced deformation, we assume a step-like stress change occurring on 23 Dec 1975, when the dike reached its final length (Buck et al. 2006). In reality, dike continues to expand slowly and to produce seismicity for weeks after the intrusion (Rivalta and Dahm 2004), so that the resulting stress rate may dominate over the tectonic spreading, similarly to what observed in Toda et al. (2002). Here we neglect this issue and postpone its consideration to a future study.

According to the rate and state theory, sudden stress perturbations cause the seismicity rate, R , to vary with time. The rate is also dependent on the Coulomb stress change, the background

rate, r , and other parameters: the secular shear stressing rate, $\dot{\tau}$, a constitutive parameter, A , and the effective normal stress, σ , which we assume constant.

$$R(t) = r \frac{1}{1 + [\exp(-\frac{\Delta CFF}{A\sigma}) - 1] \exp(-\frac{\dot{\tau}t}{A\sigma})} \quad (9)$$

(see “Appendix”). The expected number of events for a given region can be calculated by integrating the seismicity rate over time:

$$N_E(t) = r \left[t + \frac{A\sigma}{\dot{\tau}} \ln \left(1 - \left(1 - \exp \left(-\frac{\Delta CFF}{A\sigma} \right) \right) \times \exp \left(\frac{-t\dot{\tau}}{A\sigma} \right) \right) + C \right] = rt + f(t) \quad (10)$$

where

$$f(t) = r \left[\frac{A\sigma}{\dot{\tau}} \ln \left(1 - \left(1 - \exp \left(-\frac{\Delta CFF}{A\sigma} \right) \right) \times \exp \left(\frac{-t\dot{\tau}}{A\sigma} \right) \right) + C \right]$$

and C is an integration constant.

For an arbitrary time interval $\Delta t = t_2 - t_1$ with $t_1 > 0$, the number of predicted events is:

$$N_E(\Delta t) = r\Delta t + f(t_2) - f(t_1) \tag{11}$$

If we state $N_T = r\Delta t$ in Eq. 11, this represents the portion of events that occur due to background tectonic activity. Therefore, the number of events that can be attributed to just the Coulomb stress change, i.e. $N_D = N_E - N_T$, is:

$$N_D = f(t_2) - f(t_1) \tag{12}$$

A schematic representation of N_D and N_T is in Fig. 7.

Given that the Δ CFF is space dependent, the seismicity rate and number of earthquakes expected for the Dike scenario will be space dependent as well. Hence, we define a spatial seismic intensity as the number of events $n_D(x, y)$ occurring in an element of area, S of the GL box centred in the grid point (x, y) . For the Tectonic scenario, the spatial seismic intensity will be simply $n_T = r\Delta t/A_{GL}$, where A_{GL} is the total area of the GL box.

4.3 Constraining the model parameters

We need to set: (1) the background seismicity rate, r ; (2) the secular shear stressing rate, $\dot{\tau}$ and (3) the constitutive parameter for the rate-and-state friction law times the normal stress, $A\sigma$.

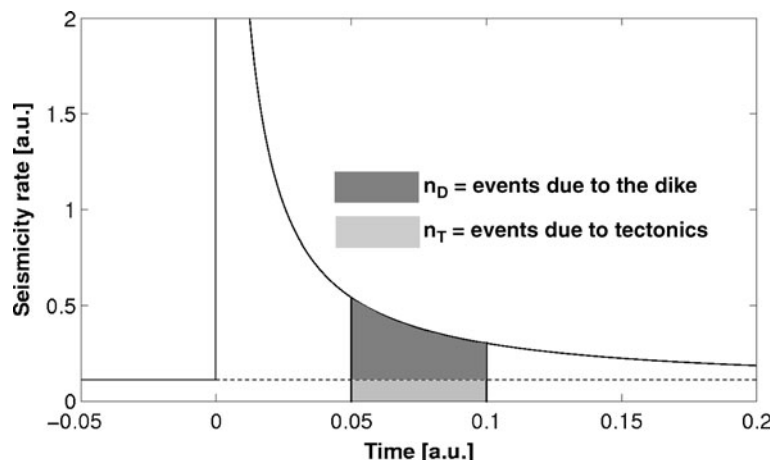
We calculate r by including all seismic events above the magnitude of completeness over the GL

(Toda and Stein 2003); see Fig. 1. Since we are not using a declustered catalogue, the term ‘reference seismicity rate’ is more appropriate than ‘background seismicity rate’ (Cocco et al. 2010). We take r as uniform over the whole region, as suggested by Cocco et al. (2010) because of the sensitivity of the rate-and-state model to inhomogeneous seismicity rates and find $r = 0.11/\text{km}^2\text{year}$. While the use of a non-uniform reference seismicity rate could reveal smaller-scale features of the dike–fault physical interaction, such a detailed model could be misleading. Unlike Cocco et al. (2010), however, we do not use a smoothed catalogue.

We calculate the secular stressing rate, $\dot{\tau}$ acting on the GL from the measured spreading rate at the TFZ, that is 20.1 mm/year, of which the GL contributes roughly 66 % towards it (Geirsson et al. 2006; Metzger et al. 2011). We assume that the shearing occurs over a distance of 40 km orthogonal to the GL. We find a stressing rate at the GL of 9.75×10^3 Pa/year.

The $A\sigma$ parameter is related to the aftershock decay time, t_a through the relationship $t_a = A\sigma/\dot{\tau}$ (Dieterich 1994). By estimating the time duration of an aftershock sequence, t_a , and the tectonic loading, $\dot{\tau}$, independently, we can directly obtain an estimate of $A\sigma$. For this purpose, we fit the modified Omori law (Utsu et al. 1995) for a $M = 4.56$ event that struck on Jan 5th 2005 in the northwestern part of the GL in the GHF; see Fig. 1. We estimate the three parameters of the modified Omori decay law through the maximum

Fig. 7 Schematic representation of the time-dependent seismicity rate (solid line) after a stress-step application at time $t = 0$. The dashed line represents the background seismicity rate. Dark gray area number of earthquakes N_D given by the dike-induced stress change only; light gray area number of earthquakes N_T given by the tectonics only



likelihood procedure proposed by Ogata (1983) in a cubic region of 15 km side beneath the epicentre of the main event (see Fig. 8). We obtain $t_a \approx 40$ days as the time interval required to return to the background seismicity level for the mainshock region. This gives $A\sigma = 1.1 \times 10^3$ Pa, which is 1 order of magnitude less compared to the value estimated by Toda et al. (2002) for the seismic swarms accompanying the Izu Islands dike intrusion, and other estimates present in literature (Cocco et al. 2010). We obtain a lower value for $A\sigma$ mainly because of the high reference background seismicity rate of the GHF, which is a site of frequent fluid-induced swarms; fitting the modified Omori law with the reference seismicity rate calculate over the whole GL gives a value of $A\sigma$ of the same order as the seismicity rate as inferred by Toda et al. (2002).

4.4 Change in seismicity rate induced by the dike intrusion

From the Coulomb stress calculation for model M4 (see Section. 3.2) calculated on a grid of squares of area $S \approx 0.5$ km², we calculate the total number of events (Eq. 11) and the spatial intensi-

ties, n_D and n_T , for the time interval of the 13 Jan 1976, when the earthquake occurred.

The modeled seismicity rate follows the spatial pattern of the Coulomb stress in the GL box, as shown in Figs. 9 and 10 for the \perp GL plane and the \parallel GL plane, respectively. The time-dependent seismicity rate of the region is also mapped at three time instants: after 7, 45 and 90 days from the diking event, as shown in Figs. 9 and 10 (upper panels). After the stress application, the seismicity rate increases by several orders of magnitude and then gradually decreases to the reference seismicity rate, over the period of aftershock decay time. Therefore, the hypothesis that all stresses induced by the dike are relieved after 10 years, and the use of the 1995–2011 seismic catalogue as reference seems to be justified. The total number of events predicted by the model in the GL region is slightly higher for the \parallel GL plane solution than for the \perp GL one. This is due to the fact that a larger area in the GL is affected by a positive Coulomb stress change when fault planes \parallel GL are considered. For both fault plane orientations, the major contribution in terms of number of events is given by the region close to the dike tip. For the day 13 Jan 1976, the model predicts a number

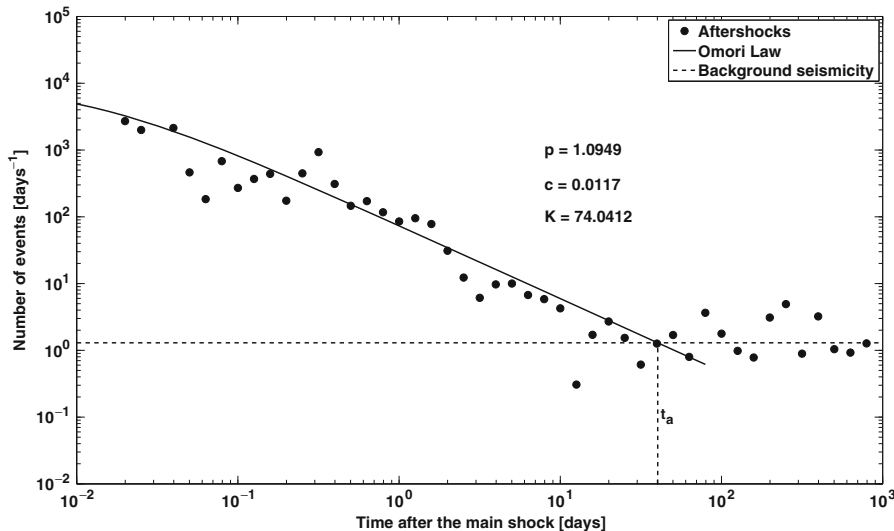


Fig. 8 Modified Omori aftershock decay law estimated by the maximum likelihood estimation (Ogata 1983). The parameters inferred are reported in the inset, the black line refers to the modified Omori law, black dots are the number of events, and the dashed line is the reference

seismicity rate. The aftershock decay time t_a is given by the intersection of the modified Omori law and the reference seismicity rate calculated in a cubic volume of 15 km side around the mainshock

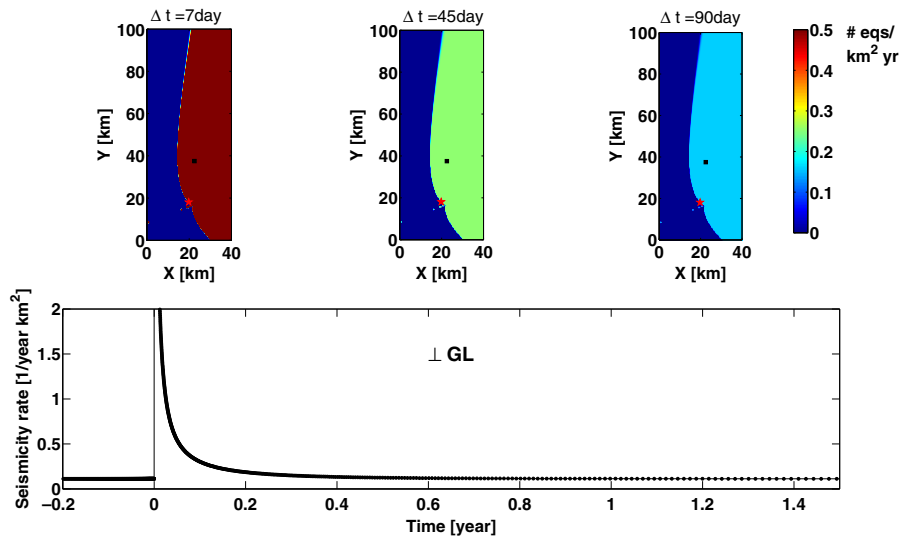


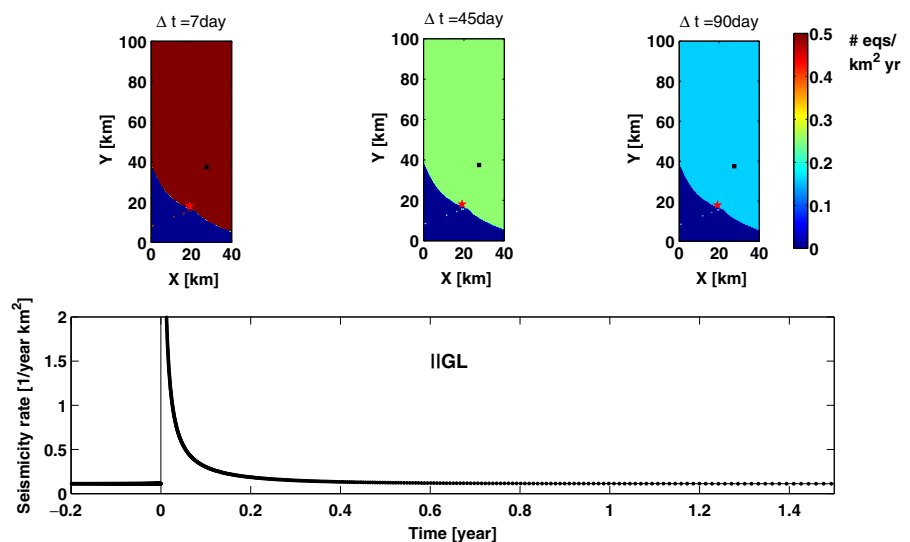
Fig. 9 Seismicity rate of $M \geq 6$ predicted by the rate and state model for the \perp GL fault plane solution. *Upper panels* seismicity rate calculated for time steps Δt of 7, 45 and 90 days; *red star* is the 13 Jan 1976 earthquake epicentre. *Lower panel* seismicity rate calculated in the location of

the *black square* in the *upper panels* for the time window $[-0.2, 5]$ years where $t = 0$ is 23 Dec 1975 (end of dike emplacement phase). The value of the Coulomb stress in the *black square* grid point is 1.27 MPa

of events with $M > M_c$ as roughly equal to 3 for the \perp GL plane and equal to 4 for the \parallel GL plane. From the Gutenberg–Richter law with parameters as in Section 4.1, the ratio between the number of earthquakes with $M \geq 6.0$ and the number of events with $M \geq M_c$ is 1.19×10^{-5} ; conse-

quently, the number of earthquakes with $M \geq 6$ predicted by the model in the same time window is $N_{\perp GL}(M \geq 6) = 3.33 \times 10^{-5}$ and $N_{\parallel GL}(M \geq 6) = 5.03 \times 10^{-5}$. In the next section, we will calculate the probability of one $M \geq 6$ event, assuming that the seismicity of the area can be described by a

Fig. 10 Same as Fig. 9 for the \parallel GL fault plane solution. The value of the Coulomb stress in the *black square* grid-point is 0.33 MPa



Poisson process in space and time (Dieterich and Kilgore 1996).

5 From the seismicity rate to the probabilistic calculation of the triggering scenario

We want now to calculate the probabilities $p(E | T)$ and $p(E | D)$ of a $M \geq 6$ earthquake occurring in the GL in the scenarios T and D . We express them through the product of two probability density functions (pdf): one for the location of the earthquake and the other for the spatially varying likelihood of earthquake occurrence for the two scenarios, as explained in detail in the next two paragraphs.

5.1 Pdf for the earthquake location

Since we do not have the error ellipse, we express the spatial pdf for the earthquake location as a bivariate Gaussian pdf $g(x, y)$. The mean of the distribution $\mu(x, y)$ represents the coordinates (x_E, y_E) of the earthquake epicentre and the covariance matrix Σ is taken diagonal with $\sigma_x = \sigma_y = 7.5$ km. We truncate the Gaussian density $g(x, y)$ at the 99.7th percentile ($\sim 3\Sigma$) so that $g(x, y)$ is defined on a circle S_c of 22.5 km radius. We then re-normalise it so that $\int_{S_c} g(x, y) dx dy = 1$.

5.2 Pdf for the probability of earthquake occurrence

We model the seismicity as a Poisson process, non-homogeneous in space (the probability to observe an earthquake is space-dependent in our model) but homogeneous in time. This implies the following assumptions:

1. The probability of observing a single event over a small time interval and area is approximately proportional to the size of that interval and area.
2. The probability of two events occurring in the same narrow time interval and area is negligible.

3. The probability of an event within a certain time interval does not change over different intervals.
4. The probability of an event in one interval or area is independent of the probability of an event in any other non-overlapping time interval or area.

These assumptions apply to our catalogue only to a certain extent; for example, earthquake clusters within the catalogue invalidate the last assumption. Also, from the historical Icelandic catalogue, we know that two other $M \geq 6$ events occurred in more than thousand years on the GL: one in 1910, about 50 km away from the 13th Jan 1976 event, and one other about 1,000 years BP. These events possibly occurred in the same location of our target earthquake suggesting an earthquake was overdue and thus invalidating hypothesis N.3 (stationarity). However, here we are considering large earthquakes, which are not clustered, and within a very small time window. We reckon these approximations are acceptable for the purpose of illustrating the approach. For studies involving smaller magnitude events, which have higher recurrence rate, the assumption of a stationary rate no longer applies. For such cases, a frequentist approach that uses the modelled time-dependent seismicity rates has to be preferred for the calculation of the probability of earthquake occurrence.

The expected number of events for a Poisson distribution with generalised intensity $\lambda(x, y, t)$ is:

$$N = \int_{\Delta t} \int_{S_c} \lambda(x, y, t) dx dy dt \tag{13}$$

for a given time interval Δt and a given spatial region S_c . The probability of occurrence of a number of events, k , is: $f(k) = N^k e^{-N} / k!$. The probability that no events occur is $p(k = 0) = e^{-N}$, thus the probability of at least one event occurring is given by:

$$p(k \geq 1) = 1 - e^{-N} \tag{14}$$

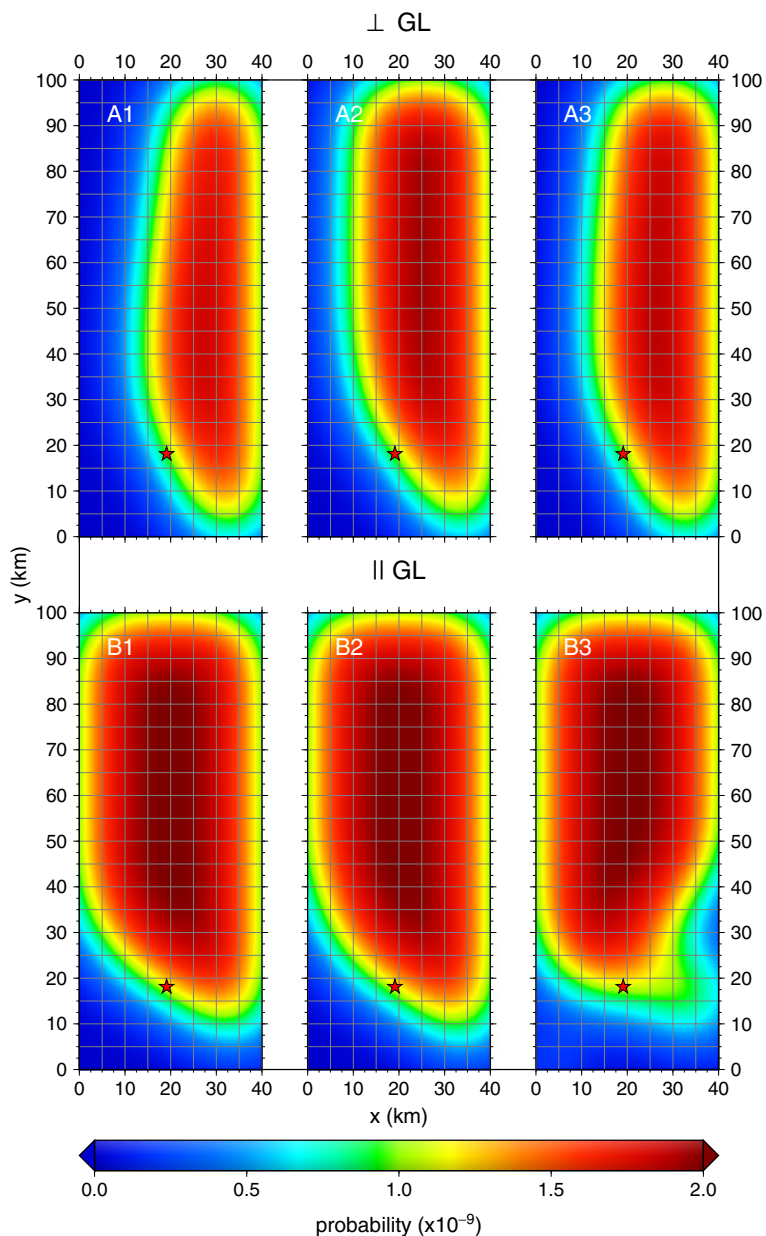
We construct the spatial probability density functions $f_D(x, y)$ and f_T for the earthquake occurrence by weighting the probability given by Eq. 14

with the spatial intensity, $n_D(x, y)$ and n_T , derived in Section 4.2 and normalising over the area A_{GL} of the GL box:

$$f_H(x, y) = \frac{n(x, y)}{\int_{A_{GL}} n(x, y) dx dy} \left[1 - e^{-\int_{A_{GL}} n(x, y) dx dy} \right] \tag{15}$$

where H is either D or T . Integrated over A_{GL} , Eq. 15 gives the Poisson probability of the occurrence of at least one event in that area. We require this spatial density function to be zero in those areas where the Coulomb stress is negative, in order for $n(x, y)$ to be positive. For the regions with stress shadowing, a different approach is needed and will be addressed in future studies.

Fig. 11 Probability maps calculated from Eq. 16. *A1, A2, A3* show the spatial probabilities for \perp GL fault solution using, respectively; ΔCFF_1 , ΔCFF_2 and ΔCFF_3 as input of the Dieterich’s model. In analogy, *B1, B2, B3* are the same but for \parallel GL obtained with ΔCFF_1 , ΔCFF_2 and ΔCFF_3 , respectively. *A1* and *B1* refer to the reference configuration used in Section 5.3. The gradients of probabilities at the edges of the GL box in all panels are artifacts due to the assumption that background seismicity rate r is set to be equal to zero outside of the GL box



5.3 Conditional probabilities

Since $g(x, y)$ and $f_H(x, y)$ are independent, the joint probability of locating an earthquake with Gaussian error $g(x, y)$ in the grid-point (x_E, y_E) given the space-dependent likelihood of that earthquake is given by:

$$p(E | H)(x, y) = \int_{S_c} g(x' - x_E, y' - y_E) f_H(x', y') dx' dy' \quad (16)$$

Next, by combining Eqs. 1 and 2 with a priori probabilities of 0.5, we calculate the probability of triggering, $p(H | E)$, of the hypotheses H conditional to E .

For hazard assessment purposes (hence before any earthquake occurs), maps of $p(E | D)(x, y)$ can be plotted as functions of a hypothetical location of a large magnitude earthquake. Therefore, Eq. 16 has to be calculated for each grid point of the studied region as plotted in Fig. 11. If the epicentre location had no error (Dirac's delta distribution), the function $p(E | H)(x, y)$ would reproduce the spatial probability distribution $f_H(x, y)$. When the location lacks accuracy, the Gaussian

distribution smooths out the spatial probability as in Fig. 11.

We pinpoint the earthquake location on the probability maps (red star in Fig. 11, panels A1 and B1). In both cases, the earthquake $M \geq 6$ in Fig. 11 has a probability of about 10^{-9} , which is 60–70 % of the maximum value. A closer look to Fig. 11 reveals that this probability map based on the Coulomb stress change in the region allows us to evaluate if the event was linked to the induced stress change simply by observing how distant its location is from the probability maximum. This procedure is more reliable if the quality of the seismic network is high because the area under consideration could be subdivided more finely for the calculation of a spatially dependent r , resulting in probability maps with higher resolution

The probability of the scenarios are obtained by substituting the probability $p(E | D)(x_E, y_E)$, resulting in $p_{\perp}(E | D) = 1.03 \times 10^{-9}$ and $p_{\parallel}(E | D) = 1.15 \times 10^{-9}$, and $p(E | T) = 6.58 \times 10^{-10}$, into Eqs. 1 and 2. The probabilities that the earthquake was triggered lead to $p_{\perp}(D | E) = 0.61$ and $p_{\parallel}(D | E) = 0.64$. We conclude that the Dike scenario is the most likely one.

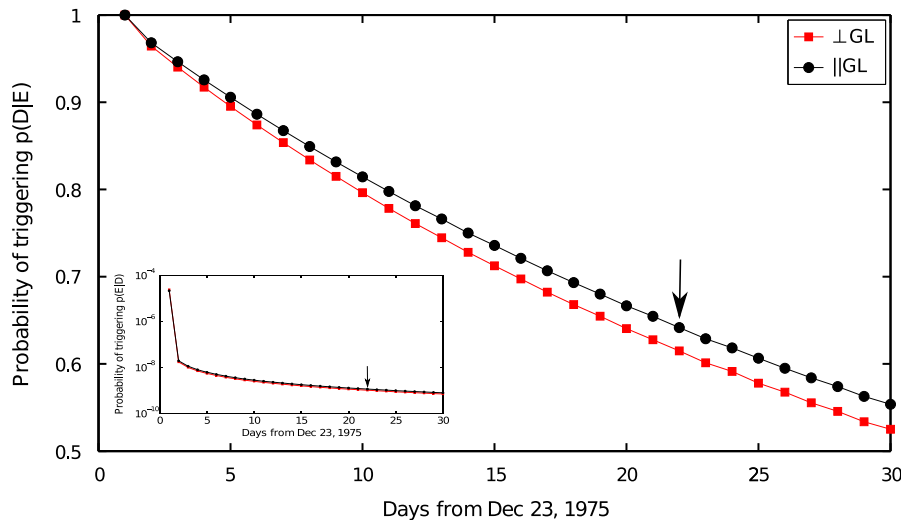


Fig. 12 Daily probability of triggering $p(D | E)$ in the first month after the instantaneous dike emplacement. The probability, $p(D | E)$, is calculated for \perp GL (squares) and \parallel GL (circle). In the inset, it is plotted the daily probability $p(E | D)$ for both \perp GL and \parallel GL fault planes, using the

same symbols as in the main plot. Both plots refer to the value of probability of the area where the K opasker earthquake epicentre falls. Arrow indicates the day of the K opasker earthquake occurrence

As already mentioned, the probability of triggering is time dependent if the seismicity modelling has a time dependency. We calculate the daily probabilities of triggering, $p_{\perp}(D | E)$ and $p_{\parallel}(T | E)$, for the first month after the diking event within the region of earthquake epicentre (Fig. 12). For the first day after the intrusion, the daily probability is very close to one; after that, the daily probability decreases approximately linearly. After 1 month from the dike emplacement, the probability is still higher than 50 %, meaning that the likelihood of the event for the dike scenario for both fault plane orientation is higher than for the tectonic scenario. The probability $p_{\perp, \parallel}(D | E)$ is higher than 50 % as long as the number of events $n_D > n_T$ and approaches zero when the predicted background rate, R , approaches r . The probability of triggering will hence approach zero only asymptotically, and a minimum cutoff value for $p(D | E)$ is needed to deem it zero.

Finally, it is worth mentioning that while the probability of triggering decreases relatively slowly with time, the probability of the event, namely $p_{\perp, \parallel}(E | D)$ plotted in the inset of Fig. 12, decreases of about 3 orders of magnitude during the first day after the dike intrusion. The absolute value of the likelihood of the event is small since we focus only on events with $M \geq 6$ in a 24-h time window and in a small spatial area of about 22 km².

6 Discussion

We find that the probability that the earthquake was triggered by the dike-induced stress change results to be about 60 % for both earthquake plane solutions. The proposed Bayesian scheme provides a straightforward way to compare and merge together different studies carried out with different methodologies on the same phenomenon.

6.1 A priori probabilities

A critical point for our formulation of the triggering probability, expressed through Eqs. 1 and 2, is to assign a reasonable and objective value to the

a priori probabilities for the studied scenarios. If no evidence is available, the a priori probability can be defined from general principles or theory; when evidence is available, the a priori probability is determined largely by that evidence rather than theoretical assumptions or logic. The posteriors from previous problems can also be used as priors for a new problem.

A poor choice of the a priori probability may have a critical impact on the final triggering probability; for instance, we may set $p(D) = 0.08$, representing the total number of earthquakes triggered globally as a lower estimate from Parsons (2002). This choice would change altogether our result for $p(D | E)$, as it would drop to about 10 %. However, that estimate considers only the shear stress contribution to earthquake triggering, while dikes induce strong compression to their sides and strong extension close to their tips. Hence, we consider the estimate inappropriate for our a priori.

6.2 Discussion of uncertainties

Hainzl et al. (2010) pointed out that several factors may cause large uncertainties in seismicity rate changes from the rate and state theory and Δ CFF calculations. In the following, we discuss the major sources of error that can propagate through our physical and statistical models by recalculating the probabilities for realistic variations of the parameters, in order to weight their relative importance. We only discuss the change in the probabilities $p_{\perp}(E | D)$ and $p_{\parallel}(E | D)$ as relative variations $\delta p_{\cdot} = \Delta p_{\cdot}(E | D) / p_{\cdot}(E | D)$ where $p_{\cdot}(E | D)$ are the probabilities calculated in the previous section that we keep as reference, the \cdot refers in turn to \perp GL and \parallel GL fault plane solution and positive and negative values of δp indicate an increase or a decrease of the probability. We report in Table 2 the changes in the value of probability for $p(E | D)$ and $p(D | E)$, for each source of error considered.

6.2.1 Uncertainties from the dike modelling

One source of error could be the position of the dike tip with respect to the epicentre location.

Table 2 Value of probabilities $p_{\perp,\parallel}(E | D)$ and $p_{\perp,\parallel}(D | E)$

	$p_{\perp}(E D) (\times 10^{-9})$	$p_{\parallel}(E D) (\times 10^{-9})$	$p_{\perp}(D E)$	$p_{\parallel}(D E)$
M1	0.99	1.12	0.60	0.63
M2	1.03	1.15	0.61	0.64
M3	1.00	1.31	0.60	0.63
ΔCFF_2	1.07	1.16	0.62	0.64
ΔCFF_3	1.06	1.07	0.62	0.62
$b = 1.08$	1.19	1.34	0.61	0.64
$b = 1.10$	0.97	1.09	0.61	0.64
$M_c = 1.3$	1.31	1.48	0.61	0.64
$A\sigma = 10^{-2}$ MPa	5.52	6.18	0.89	0.90

The first left-hand column refers to which modeling or parameter change respect to the reference triggering probability we calculate in Section 5.3, that is, dike model M4, ΔCFF_1 , $b = 1.09$, $M_c = 1.5$ and $A\sigma = 1.1 \times 10^{-3}$. The probability values for the reference configuration are $p_{\perp}(E | D) = 1.02 \times 10^{-9}$, $p_{\parallel}(E | D) = 1.15 \times 10^{-9}$, $p_{\perp}(D | E) = 0.61$ and $p_{\parallel}(E | D) = 0.64$

However, the earthquake has larger location uncertainties than the dike, so only the relative distance between dike tips and earthquake epicentre matters.

Next, we calculate the changes in the probability $p(E | D)$ when switching from model M4 (used as reference) to models M1, M2 or M3. Using model M1, we find relative changes in probability are $\delta p_{\perp} = -0.03$ and $\delta p_{\parallel} = -0.02$, model M2 gives $\delta p_{\perp} = +0.002$ and $\delta p_{\parallel} = +0.003$ and model M3 gives $\delta p_{\perp} = -0.02$ and $\delta p_{\parallel} = -0.02$. For this particular case, the variability arising from the choice of dike modelling does not affect $p(E | D)$ significantly. The reason why the opposite is found when studying earthquake-induced ΔCFF might be that the lack of friction between dike walls allows the patterns of dike-induced stress changes to be smoother than the stress changes induced by earthquakes; in other words, the distributed slip associated to faulting is in general much more irregular than the distributed opening for dike injections. Moreover, all models used here are constrained by setting a specific overpressure on the dike walls. This is preferable because more physically sound, than assigning displacement on dislocations, as is often done when modelling earthquake slip.

6.2.2 Post-diking deformation

Geodetic measurements and seismicity from the post-diking period indicate that the dike continued to expand for weeks after emplacement (Buck et al. 2006). This is often observed after dike

intrusions. In order to consider this in the modelling, the stressing rate due to the dike thickening should be compared with the tectonic stressing rate and, if larger, used in the equations controlling the production of seismicity. Alternatively, the equations of the rate and state theory (see “Appendix”) could be integrated for a series of stress changes. This would possibly have a significant effect on the final result, but it is difficult to estimate in this case, as time-dependent geodetic data for the opening of the dike are not available.

6.2.3 Coulomb failure function

Another source of uncertainty in the rate and state model is related to the calculation of the Coulomb failure function from the stress tensor components (Hainzl et al. 2010, and reference therein). Uncertainties arise from the choice of the friction coefficient and from neglecting the effects of fluids in the Coulomb failure function. We recalculate the ΔCFF with a different effective friction coefficient ($\mu = 0.4$) in Eq. 8, and we name it ΔCFF_2 . Separately, we also calculate the ΔCFF as appropriate when fluids are present:

$$\Delta\text{CFF}_3 = \sigma_s + \mu(\sigma_n + \Delta p) \tag{17}$$

where $\Delta p = -\frac{1}{3}\sigma_{kk}$ and σ_{kk} is the trace of the stress tensor.

For ΔCFF_2 , the number of expected earthquakes increase for the $\perp\text{GL}$ fault plane orientation, leading to higher values of probability.

In contrast, the \parallel GL fault plane solution seems not to be affected by the lowering of the friction coefficient value in the Coulomb stress calculation. In detail, the changes in probability values are equal to $\delta p_{\perp} = +0.05$ and $\delta p_{\parallel} = +0.01$. When considering the ΔCFF_3 , we find errors in probability of the same order of the previous ones: $\delta p_{\perp} = +0.04$ and $\delta p_{\parallel} = -0.07$. This means that the error introduced by the Coulomb stress modelling are of the same order of the ones introduced by the dislocation modelling. The \parallel GL fault plane solution is more sensitive to the presence of fluid pore pressure and less to the lowering of the friction coefficient, whereas the \perp GL seems more sensitive to both the Coulomb stress modelling. These results are consistent with the findings that \perp GL is more affected by the normal component of the dike-induced stress, while for the \parallel GL, the shear stress plays the major role in the Coulomb stress calculation. The probability maps calculated using ΔCFF_2 and ΔCFF_3 are presented in Fig. 11 (A2, A3, B2 and B3).

The uncertainties in the seismic rates arising from the stress and ΔCFF modelling are, however, likely to be very large for the first hours after the sudden stress change, as the value of ΔCFF controls the height of the seismicity peak. After a short time, the seismicity rate drops by orders of magnitude, and the impact of Coulomb stress on the total uncertainty is expected to drop.

6.2.4 Poroelastic effects

Abundance of fluids may lead to important poroelastic effects in the TFZ. The time scale of stress variations due to poroelastic flow is about 3 weeks, or possibly longer for less permeable deeper zones where the earthquake had probably nucleated (Jónsson et al. 2003). This is the same order of magnitude of the delay between the diking event and the occurrence of the earthquake, so that poroelastic effects are potentially significant. Poroelasticity amplifies the effect of the ΔCFF by first compressing and then slowly releasing the fluids in areas of σ_n increase and, to the contrary, dropping the pressure of fluids and then slowly re-increasing it in areas of dilatation. This transient effect caused by fluid migration can be mirrored in a time dependent ΔCFF of which the initial

value is given by Eq. 17 (i.e. accounting for pore pressure effects) and the final value, when the equilibrium pressure recovers, is given by Eq. 8. Therefore, the errors resulting when neglecting poroelasticity are of the same order of magnitude of those arising from the Coulomb stress calculation for the presence of fluids.

Interestingly, since the effect is mainly on σ_n and not on σ_s , only the \perp GL geometry would be affected (see Fig. 4). We conclude that this factor should decrease the probability of the \perp GL fault plane solution with respect to the \parallel GL solution.

6.2.5 Statistical uncertainties

The estimated b value of the Gutenberg–Richter law together with the magnitude of completeness, M_c , can bias the fraction of expected $M \geq 6$ events. Unfortunately, the 1995–2011 catalogue does not contain seismicity with $M \geq 4.6$, so it is difficult to evaluate the fit for higher magnitude events, although the magnitude of completeness seems well constrained. To gauge the variability introduced by the b value, we recalculate the fraction of $M \geq 6$ earthquakes for $b = 1.09 \pm 0.01$ finding a relative probability change of: $\delta p_{\perp} = \delta p_{\parallel} = -0.06$ for $b = 1.1$ and $\delta p_{\perp} = \delta p_{\parallel} = +0.16$ for $b = 1.08$. Also, we check for $M_c = 1.3$, the one at 90 % confidence level of goodness-of-fit test that yields $b = 1.07 \pm 0.01$. The larger fraction of $M \geq 6$ events and larger reference rate result in errors $\delta p_{\perp} = \delta p_{\parallel} = +0.29$. We conclude that the uncertainty related to the statistical modelling of the frequency distribution of earthquakes is larger than the other source of errors analysed so far.

6.2.6 Earthquake nucleation model

The rate and state seismicity model contains three parameters: the reference seismicity rate, r , the stressing rate, $\dot{\tau}$, and the rate and state constitutive parameter, $A\sigma$. The error introduced by r is considered negligible compared with other errors only because here we use a uniform reference seismicity rate for all GL region. Conversely, with a non-uniform r , the location error should be taken into account (Hainzl et al. 2010, and

reference therein). We are confident that the error introduced by the estimation of τ is much lower than the other source of errors due to the precise measurement of the spreading rate on the TFZ (Geirsson et al. 2006; Metzger et al. 2011) from which τ is estimated. A likely source of larger errors introduced could be due to the estimate of the aftershock Omori decay used to obtain the parameters $A\sigma$. The inferred value of $A\sigma$ is one order of magnitude lower compared with other similar estimates; see, for example, Toda and Stein (2003) for the Izu dike intrusion event and Hainzl et al. (2010) for a review. In order to test the role played by the parameter $A\sigma$ in the probability estimates, we run the model with the value found by Toda et al. (2002), i.e. $A\sigma = 10^{-2}$ MPa. This provides 1 order of magnitude increase in the number of expected events for the all GL leading to a large increase in all inferred probabilities. The variation in probability results in $\delta p_{\perp} = +4.40$ and $\delta p_{\parallel} = +4.38$. We conclude that the uncertainty on $A\sigma$ has the highest impact on the final result. This effect is time dependent: Since $A\sigma$ controls the rate of decay of the seismicity rate after the intrusion-induced peak, the impact of uncertainties on $A\sigma$ is negligible (of the same order of magnitude found for the uncertainties from the dike model) during the first hours or days after the stress change, but it increases dramatically as time elapses.

6.2.7 Time window

So far, we have performed the analysis in a 1-day time window around the actual earthquake occurrence date, i.e. about 3 weeks after the dike emplacement. In this scenario, the seismicity rate predicted by the rate and state model is dominated by the fast aftershock decay time we found and was less sensitive to the intensity of the dike-induced Coulomb stress change. In general, the choice of a short time window in retrospective triggering assessments is desirable so that the rates of induced seismicity do not vary significantly. In this and other cases, however, the small error on the occurrence time of the earthquake is coupled with a large error on the occurrence time of the stress change, and the relative impact of this uncertainty should be also checked.

In forecasting studies, all predicted seismicity from the beginning of the sequence has to be taken into account to assess the probability of a large event in the near future. In those cases, the analysis will be more sensitive to the Coulomb stress change. If our time window is enlarged to 22 days, from the dike stopping to the earthquake occurrence, the probability map from Eq. 16 for the two fault plane solution and the three different ΔCFF discussed in the text changes as shown Fig. 13. All probability maps have regions of probability maxima that reproduce the spatial pattern of the Coulomb stress change, as expected. In this case, the rate and state model predicts a larger cumulative number of $M \geq 6$ earthquakes (~ 0.2) leading to values of probability for the triggering scenario very close to one for both fault plane solutions.

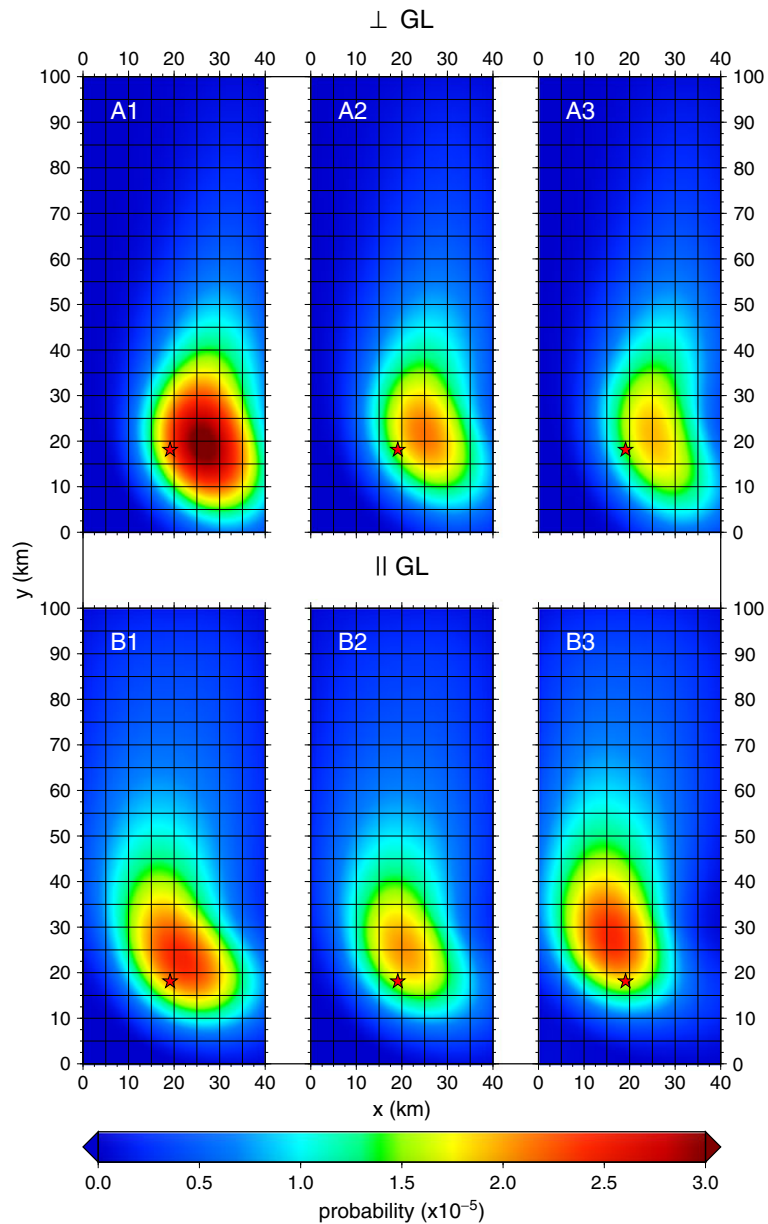
6.2.8 Summary of error analysis

In summary, the largest source of uncertainty for the present calculation is the parameter $A\sigma$, which results in an uncertainty of the probability of triggering as large as 30 % (see Table 2). The Coulomb stress model is also responsible for a significant uncertainty. The other sources of error examined above do not significantly change the probability of the triggering scenario, as they are in the range of 1–5 % (see Table 2); yet, they could play an important role when the probability of the scenarios are close to 50 %.

We stress that the errors are not independent from each other because of correlations among the variables and parameters within the various equations, which do not allow to cumulate errors (Cocco et al. 2010). We also stress that the relative importance of the various sources of error is strongly time dependent and should be checked in each case.

A full treatment of errors within the proposed methodology would allow uncertainties to propagate through the model. In principle, this can be handled through a full stochastic approach that considers the parameters and variables of the model as probability density functions. Alternatively, bootstrap techniques on the earthquake catalogue together with Monte Carlo simulation

Fig. 13 Same as Fig. 11, but with the number of expected events from the rate and state model are calculated in a time window $\Delta t = 22$ days from the dike emplacement to the earthquake occurrence date



of the parameters of the rate and state model are suitable for the same purpose.

This methodology—here used with single values of probability—can be extended to incorporate pdfs under a full Bayesian approach: In Eqs. 1 and 2, the probabilities for the likelihood and the prior distributions assume the form of pdfs. This would allow us to examine the interplay between the various sources of error and lead to a calculation of the final probability as a pdf itself.

6.3 Application to seismicity induced by human activities

As suggested above, the proposed approach can be applied in all contexts of earthquake triggering studies, including man-induced seismicity from mining, geothermal plants and gas and oil fields. For this purpose, mutually exclusive scenarios, covering all possible causes of the seismicity, need to be defined first, and Eqs. 1 and 2 need to be

extended to treat more than two scenarios. Next, several parameters and information need to be collected:

- Evidence that could be used in defining appropriate prior probabilities
- A good seismic history of the region for an accurate calculation of the background seismicity
- Accurate information on the tectonics of the area including the stressing rate
- Accurate information on the stress changes induced on the surrounding medium (obtained for example through geomechanical modelling)
- A good location for the earthquakes and their aftershocks sequences

This implies the existence of a good geophysical network well in advance of the start of the activity.

6.4 Outlook and concluding remarks

Possible improvements of the presented methodology should include a fully stochastic approach accounting for propagating uncertainties in both the physical modelling of the stress change and the statistical modeling of the seismicity. The statistical modeling should benefit from the use of a stochastic process that eliminates the bias from spatial and temporal earthquake clustering. Furthermore, a spatial non-uniform background seismicity rate should be taken into account in order to increase the resolution of the probabilistic hazard maps. Finally, we considered here the dike intrusion as a static process, but it is desirable in future studies to consider the stressing rate induced by a dynamic dike emplacement due to post-diking expansion and the consequent weakening and stressing of the surrounding rocks.

Acknowledgements This work was funded by an European Research Council Starting Grant, project CCMP-POMPEI. Seismic data are from SIL network of the Icelandic Meteorological Office. Sebastian Heimann and Martin Hensch provided useful advice on the data. We thank Dirk Becker for fruitful discussion on the seismicity model; we are also indebted to Maria Elina Belardinelli and Marco Beleggia for useful comments on an early version of this paper. Hannah Bentham helped with proof correction. Figures 1 and 11 were plotted using Generic Mapping Toolbox by Wessel and Smith (1998).

Appendix: Rate-and-state earthquake nucleation model

The rate-and-state earthquake nucleation model relates earthquake production per unit area on a population of faults to the evolution of a state variable, γ :

$$R = \frac{dN}{dt} = \frac{r}{\gamma \dot{\tau}} \tag{18}$$

where N is the number of events per unit area in the time interval $[0, T]$. For a constant shear stressing rate, γ is equal to $\gamma_0 = 1/\dot{\tau}$, which yields $R = r$ (steady state): The seismicity rate remains at its constant background value until an external stress perturbation intervenes. The state variable γ evolves with time as:

$$d\gamma = \frac{1}{A\sigma} (dt - \gamma dS) \tag{19}$$

where A is a constitutive parameter, σ is the effective normal stress and $dS = \Delta CFF$ is the Coulomb stress change (Eq. 8). Step-like stress perturbations are accounted for by setting $dt = 0$ in Eq. 19 and integrating:

$$\gamma_1 = \gamma_0 \exp\left(\frac{-dS}{A\sigma}\right) \tag{20}$$

where γ_1 and γ_0 are the state variable values before and after the stress perturbation, respectively. By substituting Eqs. 20 in 18 and eliminating the variable γ , the peak in seismicity rate right after the stress change is obtained explicitly:

$$R_1 = r \exp\left(\frac{\Delta CFF}{A\sigma}\right) \tag{21}$$

After a step-like stress change, the tectonic stressing rate dominates in controlling the seismicity rate, which experiences a transient until it reaches again steady state. Setting $dS = \dot{\tau} dt$ Eq. 19 and integrating:

$$\gamma(t) = \frac{1}{\dot{\tau}} + \left(\gamma_1 - \frac{1}{\dot{\tau}}\right) \exp\left(-\frac{\Delta t \dot{\tau}}{A\sigma}\right) \tag{22}$$

which implies that the time needed for R to return to steady state is inversely proportional to $\dot{\tau}$. The

state variable γ can be eliminated by combining Eqs. 18, 20 and 22:

$$R(t) = r \frac{1}{1 + \left[\exp\left(-\frac{\Delta CFF}{A\sigma}\right) - 1 \right] \exp\left(-\frac{t}{A\sigma}\right)} \quad (23)$$

The expected number of events for a given region in a time window $\Delta t = t_2 - t_1$ can be calculated by integrating the seismicity rate over the time interval:

$$N_E(\Delta t) = \int_{t_1}^{t_2} R(t) dt. \quad (24)$$

References

- Bender B (1983) Maximum likelihood estimation of b values for magnitude grouped data. *Bull Seismol Soc Am* 73:831–851
- Björnsson A (1985) Dynamics of crustal rifting in NE Iceland. *J Geophys Res* 90 (B12):10.151–10.162
- Buck W, Einarsson P, Brandsdóttir B (2006) Tectonics stress and magma chamber size as controls on dike propagation: constraints from the 1975–1984 Krafla rifting episode. *J Geophys Res* 111:B12,404. doi:10.1029/2005JB003879
- Cayol V, Dieterich J, Okamura A, Miklius A (2000) High magma storage rates before the 1983 eruption of Kilauea, Hawaii. *Science* 288(5475):2343–2346. doi:10.1126/science.288.5475.2343
- Cesca S, Rohr A, Dahm T (2011) Discrimination of induced seismicity by full moment tensor inversion and decomposition. *J Seismol*, this issue
- Cocco M, Hainzl S, Catalli F, Enescu B, Lombardi A, Woessner J (2010) Sensitivity study of forecasted aftershock seismicity based on Coulomb stress calculation and rate- and state-dependent frictional response. *J Geophys Res* 115:B05,307. doi:10.1029/2009JB006838
- Dahm T (2000) Numerical simulations of the propagation path and the arrest of fluid-filled fractures in the Earth. *Geophys J Int* 141:623–638
- Dieterich J (1994) A constitutive law for rate of earthquake production and its application to earthquake clustering. *J Geophys Res* 99(B2):2601–2618
- Dieterich J, Kilgore B (1996) Implications of fault constitutive properties for earthquake prediction. *Proc Natl Acad Sci U S A* 93:3787–3794
- Dieterich J, Cayol V, Okubo P (2000) The use of earthquake rate changes as a stress meter at Kilauea Volcano. *Nature* 408:457–460
- Einarsson P (1987) Compilation of fault plane solutions in the North Atlantic and Arctic Oceans. In: Kasahara K (ed) *Recent plate movements and deformation, geodyn. ser.*, vol 20. AGU, Washington, DC, pp 47–62
- Einarsson P, Brandsdóttir B (1980) Seismological evidence for lateral magma intrusion during the July 1978 deflation of the Krafla volcano in NE Iceland. *J Geophys* 47:160–165
- Feuillet N, Cocco M, Musumeci C, Nostro C (2006) Stress interaction between seismic and volcanic activity at Mt Etna. *Geophys J Int* 164:697–718. doi:10.1111/j.1365-246X.2005.02824.x
- Geirsson H, Arnadóttir T, Volksen C, Jiang W, Sturkell E, Villemin T, Einarsson P, Sigmundsson F, Stefansson R (2006) Current plate movements across the Mid-Atlantic Ridge determined from 5 years of continuous GPS measurements in Iceland. *J Geophys Res* 111:B09,407. doi:10.1029/2005JB003717
- Hainzl S, Steacy S, Marsan D (2010) Seismicity models based on Coulomb stress calculations. Community online resource for statistical seismicity analysis (CORSSA). doi:10.5078/corssa-32035809. <http://www.corssa.org>
- Halldórson P (2005) *Jardskjálftavirkni á Nordurlandi, Icelandic Meteorological Office. Report 05021-VÍ-ES-10*. <http://www.vedur.is/utgafa/greinargerdir/2005>
- Harris RA (1998) Introduction to special section: stress triggers, stress shadows, and implications for seismic hazard. *J Geophys Res* 103(24):347–24
- Hensch M, Riedel C, Reinhardt J, T D (2008) Hypocenter migration of fluid-induced earthquake swarms in the Tjörnes Fracture Zone (North Iceland). *Tectonophysics* 447(1–4):80–94
- Hill DP (1977) A model for earthquake swarms. *J Geophys Res* 82(8):1347–1352. doi:10.1029/JB082i008p01347
- Hill DP, Pollitz F, Newhall C (2002) Earthquake–volcano interactions. *Phys Today* 55:41–47. doi:10.1063/1.1535006
- Jacques E, King G, Tapponnier P, Ruegg J, Manighetti I (1996) Seismic triggering by stress change after the 1978 events in the Asal Rift, Djibouti. *Geophys Res Lett* 23(18):2481–2484
- Jónsson S, Segall P, Pedersen R, Björnsson G (2003) Post-earthquake ground movements correlated to pore-pressure transients. *Nature* 424(6945):179–183. doi:10.1038/nature01776
- King GCP, Cocco M (2000) Fault interaction by elastic stress changes: new clues from earthquake sequences. *Adv Geophys* 44:1–36
- Lengliné O, Marsan D, Got JL, Pinel V, Ferrazzini V, Okubo PG (2008) Seismicity and deformation induced by magma accumulation at three basaltic volcanoes. *J Geophys Res* 113:B12,305. doi:10.1029/2008JB005937
- Maccaferri F, Bonafede M, Rivalta E (2010) A numerical model of dyke propagation in layered elastic media. *Geophys J Int* 180:1107–1123
- Metzger S, Jónsson S, Geirsson H (2011) Locking depth and slip-rate of the Húsavík Flatey fault, North Iceland, derived from continuous GPS data 2006–2010. *Geophys J Int* 187(2):564–576. doi:10.1111/j.1365-246X.2011.05176.x
- Ogata Y (1983) Estimation of the parameters in the modified Omori formula for aftershock frequencies by the maximum likelihood procedure. *J Phys Earth* 31:115–124

- Parsons T (2002) Global Omori law decay of triggered earthquakes: large aftershocks outside the classical aftershock zone. *J Geophys Res* 107:B9, 2199
- Riedel C, Petersen T, Theilen F, Neben S (2003) High b -value in the leaky segment of the Tjörnes fracture zone north of Iceland: are they evidence for shallow magmatic sources? *J Volcanol Geotherm Res* 128:15–29. doi:[10.1016/S0377-0273\(03\)00244-0](https://doi.org/10.1016/S0377-0273(03)00244-0)
- Riedel C, Tryggvason A, Dahm T, Stefansson R, Bodvarson R, Gudmundsson G (2005) The seismic velocity structure north of Iceland from joint inversion of local earthquakes data. *J Seismol* 9:383–404
- Rivalta E, Dahm T (2004) Dyke emplacement in fractured media: application to the 2000 intrusion at Izu islands, Japan. *Geophys J Int* 157:283–292
- Rögnvaldsson ST, Gudmundsson A, Slunga R (1998) Seismotectonic analysis of the Tjörnes fracture zone, an active transform fault in north Iceland. *J Geophys Res* 103(B12):30,117–30,129
- Segall P, Desmarais E, Shelly D, Miklius A, Cervelli P (2006) Earthquake triggered by silent slip events on Kilauea Volcano, Hawaii. *Nature* 442:71–74. doi:[10.1038/nature04938](https://doi.org/10.1038/nature04938)
- Shi Y, Bolt B (1982) The standard error of the magnitude-frequency b value. *Bull Seismol Soc Am* 72(5):1677–1687
- Stefansson R, Gudmundsson G, Halldorsson P (2008) Tjörnes fracture zone. New and old seismic evidences for the link between the North Iceland rift zone and the Mid-Atlantic ridge. *Tectonophysics* 447:117–126
- Stein RS (1999) The role of stress transfer in earthquake occurrence. *Nature* 402:605–609
- Toda S, Stein R (2003) Toggling seismicity by the 1997 Kagoshima earthquake couplet: a demonstration of time-dependent stress transfer. *J Geophys Res* 108:B122,567. doi:[10.1029/2003JB002557](https://doi.org/10.1029/2003JB002557)
- Toda S, Stein R, Sagiya T (2002) Evidence from the AD 2000 Izu islands earthquake swarm that stressing rate governs seismicity. *Nature* 419:58–61
- Tryggvason E (1984) Widening of the Krafla fissure swarm during the 1975–1981 volcano-tectonic episode. *Bull Volcanol* 47(1):47–69
- Utsu T, Ogata Y, Matsu'ura S (1995) The centenary of the Omori formula for a decay law of aftershock activity. *J Phys Earth* 43:1–33
- Wessel P, Smith WHF (1998) New, improved version of the generic mapping tools released. *EOS Trans AGU* 79:579
- Wiemer S, Wyss M (2000) Minimum magnitude of completeness in earthquake catalogs: examples from Alaska, the Western United States, and Japan. *Bull Seismol Soc Am* 90:859–869